



Temperature dependence of [100](010) and [001](010) dislocation mobility in natural olivine



Lin Wang^{a,*}, Stephan Blaha^a, Zsanett Pintér^a, Robert Farla^a, Takaaki Kawazoe^a, Nobuyoshi Miyajima^a, Katsuyoshi Michibayashi^b, Tomoo Katsura^a

^a Bayerisches Geoinstitut, University of Bayreuth, 95440 Bayreuth, Germany

^b Institute of Geosciences, Shizuoka University, Shizuoka 422-8529, Japan

ARTICLE INFO

Article history:

Received 16 November 2015

Received in revised form 2 February 2016

Accepted 12 February 2016

Editor: J. Brodholt

Keywords:

dislocation recovery

olivine fabric

slip system

temperature dependence

seismic anisotropy

ABSTRACT

Dislocation recovery experiments were conducted on pre-deformed olivine single crystals at 1450 to 1760 K, room pressure, and oxygen partial pressures near the Ni–NiO buffer to determine the annihilation rates for [100] and [001] dislocations on the (010) plane. Olivine single crystals were first deformed to activate the desired slip systems under simple shear geometry and then annealed at target conditions. The edge and screw dislocations with Burgers vectors, \mathbf{b} , of [100] and [001], respectively, both elongated in the [001] direction were produced by the deformation. The dislocation annihilation rate constants of both types of dislocations are identical within 0.3 log unit. The activation energies for both dislocations are also identical, i.e., ~ 400 kJ/mol, which is also identical to that of the Si self-diffusion coefficient. This correspondence suggests that olivine dislocation creep controlled by a diffusion-controlled process under low-stress and high-temperature conditions. This study offers a potential insight into the formation of AG-type fabric in olivine.

© 2016 Elsevier B.V. All rights reserved.

1. Introduction

Formation of lattice preferred orientation (LPO) in mantle minerals is a consequence of the dominant slip systems activated by dislocation creep. Dominant slip system changes depending on chemical and physical conditions (Karato, 2008). Therefore, knowledge of conditions of LPO formation is useful to understand the chemical and physical conditions in the Earth's interior. In addition, LPO causes seismic anisotropy, which provides insight into the direction of upper mantle convective flow by combining observations about seismic anisotropy and conditions of formation of LPO in mantle minerals.

A number of seismic studies have shown seismic anisotropy in the upper mantle (Dziewonski and Anderson, 1981; Montagner and Kennett, 1996; Gung et al., 2003; Nettles and Dziewoński, 2008; Visser et al., 2008). These studies showed that the magnitude of seismic anisotropy decreases with depth. For example, the frequently cited one-dimensional global model, PREM (Dziewonski and Anderson, 1981), demonstrated that anisotropy in V_s and V_p gradually diminishes with depth. Montagner and Kennett (1996) suggested that horizontally polarized S-wave velocity (V_{SH}) is

faster than vertically polarized S-wave velocity (V_{SV}) at the shallow part (<250 km) of the upper mantle, but this difference decreases with depth. Visser et al. (2008) reported similar results.

Since olivine is the most abundant mineral in the Earth's upper mantle, the LPOs of olivine from natural specimens and experimentally deformed samples have been extensively studied (Karato, 1988; Jung and Karato, 2001; Katayama et al., 2004; Katayama and Karato, 2006; Ohuchi et al., 2011; Jung et al., 2006). An abundance of olivine in peridotite, originating from the deep lithosphere and upper mantle, shows concentrations on the \mathbf{a} -axis in the direction of lineation and \mathbf{b} -axis in the direction normal to the foliation (e.g., Ben Ismail and Mainprice, 1998; Nicolas et al., 1971; named as A-type fabric after Jung and Karato, 2001). Peridotites from convergent boundaries (e.g., Dobrzhinetskaya et al., 1996; Mizukami et al., 2004; Skemer et al., 2006) show concentrations on the \mathbf{c} -axis in the direction of lineation and the \mathbf{b} -axis in the direction normal to the foliation (named as B-type fabric after Jung and Karato, 2001). AG-type fabric (Ben Ismail and Mainprice, 1998, categorized by Mainprice, 2007), in which the \mathbf{a} - and \mathbf{c} -axes show a girdle structure parallel to the foliation with concentration on the \mathbf{b} -axis normal to the foliation, were also found in upper mantle samples (Michibayashi and Mainprice, 2004; Hidas et al., 2007; Satsukawa et al., 2011). These natural olivine fabrics have been reproduced in deformation experiments under different chemical and physical conditions (Jung and Karato, 2001;

* Corresponding author.

E-mail address: lin.wang@uni-bayreuth.de (L. Wang).

Holtzman et al., 2003; Karato, 2008). A-type fabric forms under high-temperature conditions and B-type fabric forms under low-temperature and/or high-stress conditions (Jung and Karato, 2001; Karato, 2008). AG-type fabric forms with coexistence of melt (Holtzman et al., 2003).

However, we note that olivine LPO fabrics obtained in the laboratory generally formed under higher stresses and many orders of magnitude higher strain rates (Hirth and Kohlstedt, 2003). Competition between dislocation glide and climb and slip system activation under those conditions may not be the same as under low stress, moderate to high temperature conditions in the Earth. Therefore, it is necessary to investigate the origin of these fabrics using a different strategy.

Orowan's equation (Hull and Bacon, 2011) is a simple formula to describe dislocation creep, in which the dislocation creep rate is a product of the Burgers vector, average mobile dislocation density, and average mobile dislocation velocity. Generally, the average mobile dislocation velocity is the product of average dislocation mobility, which is independent of force, and a function of force acting on dislocations per unit length. Therefore, compared with dislocation velocity, dislocation mobility is more representative to express the rheology property of a material. This study focuses on variations in climb mobility in edge dislocation and cross slip mobility in screw dislocations, among different slip systems as function of temperature. Although glide velocity contribute much larger to the total strain, the climb/cross slip velocity is typically much slower than glide velocity. Therefore, dislocation climb/cross slip are the rate limiting process for olivine deformation (Poirier and Vergobbi, 1978) and should control the temperature and pressure dependence of strain rate. Thus, whether temperature and pressure can cause fabric transition is determined by the temperature and pressure dependences of climb/cross slip in different slip systems. Since climb and cross slip are controlled by thermal activated processes, we investigate the temperature dependence of them in two different slip systems. Hereafter, we use dislocation mobility to refer dislocation climb/cross slip mobility and use dislocation motion to refer climb in edge dislocation and cross slip in screw dislocation.

Dislocation recovery is one experimental technique to estimate dislocation mobility. In this technique, a sample containing a certain dislocation density is annealed under hydrostatic conditions, causing a reduction in dislocation density due to annihilation. The rate constant of dislocation annihilation should be proportional to the dislocation mobility. The primary advantage of this technique is that no external stresses, which are many orders of magnitude higher in deformation experiments than in natural conditions, are applied. Hence, the physical environment in annealing experiments is more representative of the mantle than those in the deformation experiments. Another advantage of this method is that it allows much wider physical and chemical conditions than the deformation experiments, making it possible, for example, to precisely determine temperature dependence. Strictly speaking, the dislocation annihilation rate is not identical to the dislocation velocity in dislocation creep, because the driving force of dislocation annihilation is the internal stress field created by dislocations themselves, whereas the dislocation motion in dislocation creep is driven by external stresses. However, we assume that the temperature derivatives over their absolute values are identical between the dislocation motions by annihilation and the creep. In other words, the activation energies are identical for these two cases.

The A-, B-, and AG-type fabrics are the most common fabrics in nature and should be produced by the [100](010) slip system, which is called *a*-slip in this study, and/or the [001](010) slip system, which is called *c*-slip in this study. Therefore, we conducted dislocation recovery experiments on oriented single crystal olivine deformed producing *a*- and *c*-slips at ambient pressure

and temperatures of 1455 to 1763 K. The experimental results obtained in this study provide information on the temperature dependence of dislocation mobility for the most important olivine slip systems. They also offer insights into the nature of dislocation motion under low-stress conditions. Although there are many studies on dislocation recovery of olivine at high temperatures and pressures (Goetze and Kohlstedt, 1973; Kohlstedt et al., 1980; Karato and Ogawa, 1982; Karato et al., 1993; Farla et al., 2011), there is currently no study to compare dislocation annihilation rates and their temperature dependences between *a*- and *c*-slip systems. Therefore, this study provides unique data to investigate dislocation processes in the upper mantle rheology.

2. Experimental procedure

2.1. Sample preparation

The samples used in this study are single crystals of natural olivine from Pakistan. The same olivine has been describe by Gose et al. (2010) and the major and trace element, including water content, of the olivine has been reported there. The b-axis orientation of each crystal was determined using a Huber single-crystal diffractometer operated by SINGLE2014 (Angel and Finger, 2011). The oriented olivine crystals were mounted in epoxy resin with the (010) plane exposed to the surface and then polished using diamond powder with a grain size of 0.25 μm . The [100] and [001] directions were determined via electron backscattered diffraction (EBSD) in the scanning electron microscope (SEM). Cubes with 1.5 mm edge length were shaped from the oriented crystal along its crystallographic planes. The orientations of the crystals were checked again by EBSD after shaping the crystals. For the next step, inclusion- and crack-free cubes were handpicked under an optical microscope.

2.2. Production of high dislocation densities

High dislocation densities with dislocations of either [100] or [001] Burgers vector on the (010) plane were produced by experimental deformation in a Kawai-type multi-anvil apparatus at a pressure of 3 GPa and a temperature of 1600 K. Fig. 1 shows the experimental setup. A cubic hole was made at the center of an MgO slice to accommodate the cubic olivine crystal in a unique orientation. The MgO slice with the olivine crystal was sandwiched between two crushable alumina pistons, cut at an angle of 45° for simple shear deformation of the olivine single crystal. The shear geometry was in the [100] or [001] direction on the (010) plane for producing dislocations from the *a*- or *c*-slips, respectively. The sample and pistons were placed in a Pt tube, and another two columns of crushable alumina were placed on both ends of the inner crushable alumina pistons. Tungsten carbide anvils with 17 mm truncated edge lengths were used to generate high pressure together with a Cr₂O₃-doped MgO octahedron with a 25 mm edge length as a pressure medium. The furnace comprises a stepped cylindrical graphite heater and a ZrO₂ thermal insulator. Sample pressures were estimated from the hydraulic oil pressure based on calibrations using the phase transitions of Bi and Mg₂SiO₄ polymorphs. Temperatures were measured using a W97%Re3%–W75%Re25% thermocouple whose junction was located near the end of one of the alumina pistons.

The cell assembly was first pressurized to 3 GPa using a press load of 3.7 MN at ambient temperature for 2 h. The temperature was then increased to 1600 K for 15 min. The target temperature and press load were kept constant for 15 min to sinter the crushable alumina. The sample was then further compressed to a press load of 3.9 MN for 15 min to deform the sample. After deformation, the sample was quenched by switching off the heating power, and then decompressed to ambient pressure for more than 16 h.

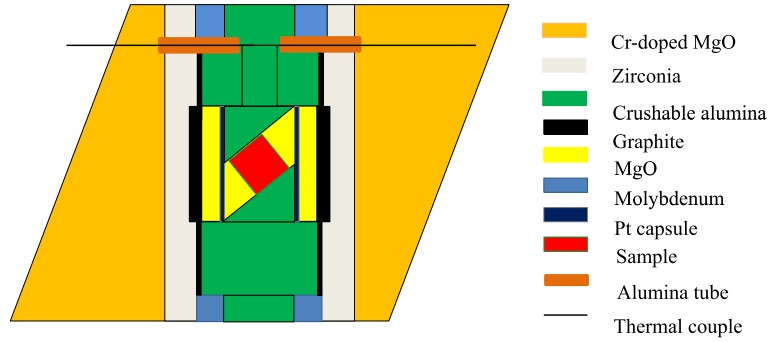


Fig. 1. The sample assembly used in the multi-anvil high-pressure deformation experiments.

After decompression, the pressure medium with the sample was polished to expose the (010) plane of the olivine crystal to examine the deviation of the crystallographic orientation from the shear direction via EBSD. The shear direction was determined using the long axis of the MgO slice. The deviations were found to be less than 3° (Fig. 2).

2.3. Dislocation annihilation by annealing

Each deformed olivine crystal was cut into eight cubic pieces. At early stages of this study, one of them was used to determine the initial dislocation density and the others were used for annealing experiments. Later, in order to minimize the uncertainty in annihilation rate constant caused by heterogeneous distribution of initial dislocations, four pairs were made from the eight pieces, where each piece shared a common (001) plane. One piece from each pair was used to determine the initial dislocation density, while the other was used to determine it after the annealing. The annealing experiment was conducted at ambient pressure and temperatures of 1460–1760 K for 20 min to 24.5 h using a gas mixing furnace. Oxygen partial pressure was controlled at 10^{-6} – 10^{-8} MPa, which was near the Ni–NiO buffer, using a CO–CO₂ gas mixture. Table 1 summarizes the conditions of the annealing experiment.

2.4. Measurement of dislocation density

Dislocations were observed using the oxidation decoration technique (Kohlstedt et al., 1976; Karato, 1987). For this method, the samples were first heated at a temperature of 1170 K for 1 h in air to oxidize dislocations. The sample surface was subsequently polished using 0.25 μm diamond powder to remove the surface Fe-oxide layer, and then observed in back-scattered electron images (BEI) by SEM at around 10 mm working distance, accelerating voltage of 10 kV, and aperture of 120 μm . Dislocations appeared as bright spots or lines by concentration of ferric iron produced by the oxidation in dislocation cores. For the paired sample, the corresponding areas in the initial and annealed pieces were observed to determine change in dislocation density caused by the annealing. We counted the [100](010) edge dislocations and [001](010) screw dislocations in *a*- and *c*-slips sample, respectively on (001) plane. On this plane, these dislocations intersect orthogonally and appear as dot contrast. The dislocation density was calculated from the number of intersecting dislocations per area following Karato et al. (1993). This method allows us to avoid the geometrical complications of dislocation density measurements taken as cumulative line lengths per unit volume. The number of dots was determined using ImageJ image processing software (<http://rsbweb.nih.gov/ij/>). We applied a contrast threshold and then automatically counted the number of particles/dislocations per area. If the raw images were not sharp enough for the software to identify the dislocations as individual particles, we manually counted the number of dislocations.

2.5. TEM observation

In order to identify the nature of the dislocations produced by *a*- and *c*-slips, two additional deformation runs were conducted (Z1031 and Z1054), and analyzed via transmission electron microscopy (TEM). The samples were double side polished with thicknesses ranging from 23 to 35 μm and fixed on glass slides. After removing the selected olivine grains from the glass slide, an Ar ion-milling method was used to make the sample thinner, using 4.5–5 kV voltages, 4–8° angles from top and bottom ion-bombardment, and total thinning times varying between 14 and 25 h depending on the thicknesses and size of each sample. TEM observations were performed using Philips CM20FEG TEM, operating at 200 kV. Dislocation microstructures were examined by dark field (DF, Bragg condition, deviation parameter, $s = 0$) and weak-beam dark field (WBDF, $s > 0$) imaging and selected area electron diffraction (SAED). We chose diffraction vectors with $\mathbf{g} = 400$ and 004 to observe dislocations with Burgers vectors $\mathbf{b} = [100]$ and $[001]$ on the (010) plane, respectively. When $\mathbf{g} \cdot \mathbf{b} = \text{integer}$, dislocations are visible by diffraction contrast.

2.6. Data reduction

Because dislocation annihilation should occur through coalescence of two dislocations with opposite signs, the dislocation annihilation rate is expected to be proportional to the dislocation density squared (Li, 1966; Toriumi and Karato, 1978). The fundamental equation for the dislocation annihilation is therefore:

$$\frac{d\rho}{dt} = -k \cdot \rho^2 \quad (1)$$

where ρ is the dislocation density, $d\rho/dt$ is annihilation rate, k is the annihilation rate constant. By solving this equation, we have

$$k = \frac{\frac{1}{\rho_f} - \frac{1}{\rho_i}}{t}, \quad (2)$$

where ρ_f and ρ_i are the dislocation density after and before annealing, respectively, and t is the annealing time. Because of the thermally activated process, the dislocation annihilation rate constant follows an Arrhenius relationship:

$$k = k_0 \exp\left(-\frac{E}{RT}\right) \quad (3)$$

where k_0 is a constant, E is the activation energy of the dislocation annihilation, T is the temperature, and R is the gas constant. As mentioned previously, E is also considered identical to the activation energy of the dislocation climb/cross slip.

3. Results

Table 1 shows the experimental results together with the annealing conditions. Fig. 3 shows BEIs of the decorated dislocations

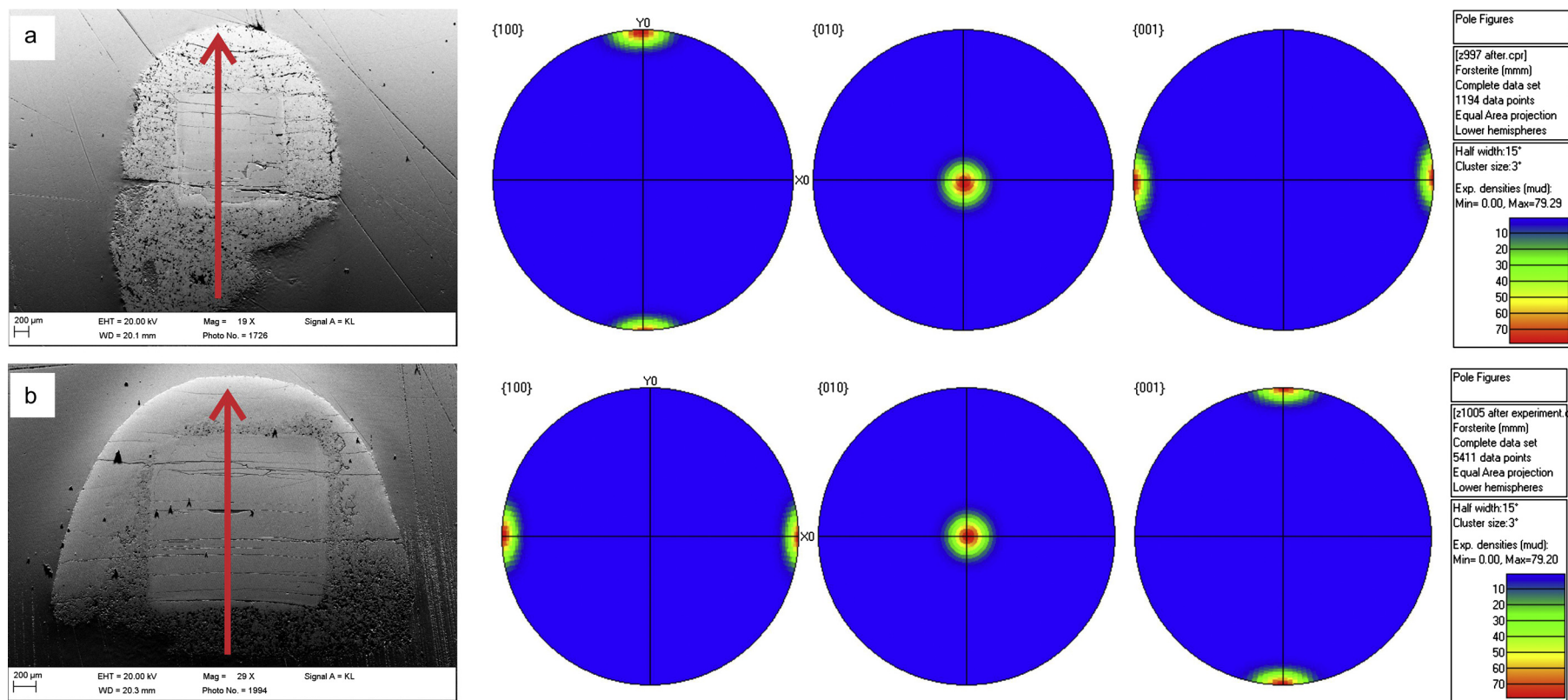


Fig. 2. Relations between the crystallographic orientation and shear direction for (a) **a**-deformed olivine and (b) **c**-deformed olivine. The red arrows show the shear direction. The deviations in crystallographic orientation from the shear directions are less than 3° . (For interpretation of the references to color in this figure legend, the reader is referred to the web version of this article.)

Table 1
Summary of experiment results.

Sample	T (K)	Annealing time (h)	$\log(f_{O_2}, 10^{-5} \text{ Pa})$	ρ_i (μm^{-2})	ρ_f (μm^{-2})	$\log(k, \text{m}^2 \text{s}^{-1})$
[100](010) edge dislocation						
Z1238-1 ^b	1763	0.4	-4.9	0.23 ± 0.08	0.15 ± 0.01	-14.8 ± 0.3
Z997-1 ^a	1748	0.3	-4.9	2.13 ± 0.25	0.79 ± 0.19	-15.2 ± 0.2
Z1238-2 ^b	1673	2.5	-5.7	0.19 ± 0.03	0.15 ± 0.03	-15.8 ± 0.5
Z1238-3 ^b	1573	11.5	-6.6	0.21 ± 0.05	0.17 ± 0.04	-16.5 ± 0.7
Z997-2 ^a	1553	1.3	-6.6	2.13 ± 0.25	1.81 ± 0.15	-16.8 ± 0.4
Z997-3 ^a	1455	24.5	-7.7	2.13 ± 0.25	1.17 ± 0.05	-17.4 ± 0.1
[001](010) screw dislocation						
Z1240-1 ^b	1763	0.4	-4.9	0.19 ± 0.06	0.08 ± 0.02	-14.3 ± 0.2
Z1005-1 ^a	1748	0.5	-4.9	0.76 ± 0.07	0.15 ± 0.04	-14.6 ± 0.1
Z1240-2 ^b	1673	2.5	-5.7	0.36 ± 0.18	0.07 ± 0.02	-14.9 ± 0.1
Z1005-2 ^a	1648	3	-5.7	0.76 ± 0.07	0.10 ± 0.04	-15.1 ± 0.2
Z1240-3 ^b	1573	11.5	-6.6	0.31 ± 0.06	0.12 ± 0.03	-15.9 ± 0.2
Z1240-4 ^b	1473	25	-7.7	0.31 ± 0.19	0.21 ± 0.03	-16.8 ± 0.6
Z1005-3 ^a	1455	24	-6.6	0.76 ± 0.07	0.33 ± 0.07	-16.7 ± 0.2

^a The experimental runs from which one of the deformed piece was used to determine the initial dislocation density while others used to determine the dislocation density after annealing.

^b The experimental runs from which one pair of deformed pieces with common (001) plane were used to determine initial and annealed dislocation density. Explanation see text.

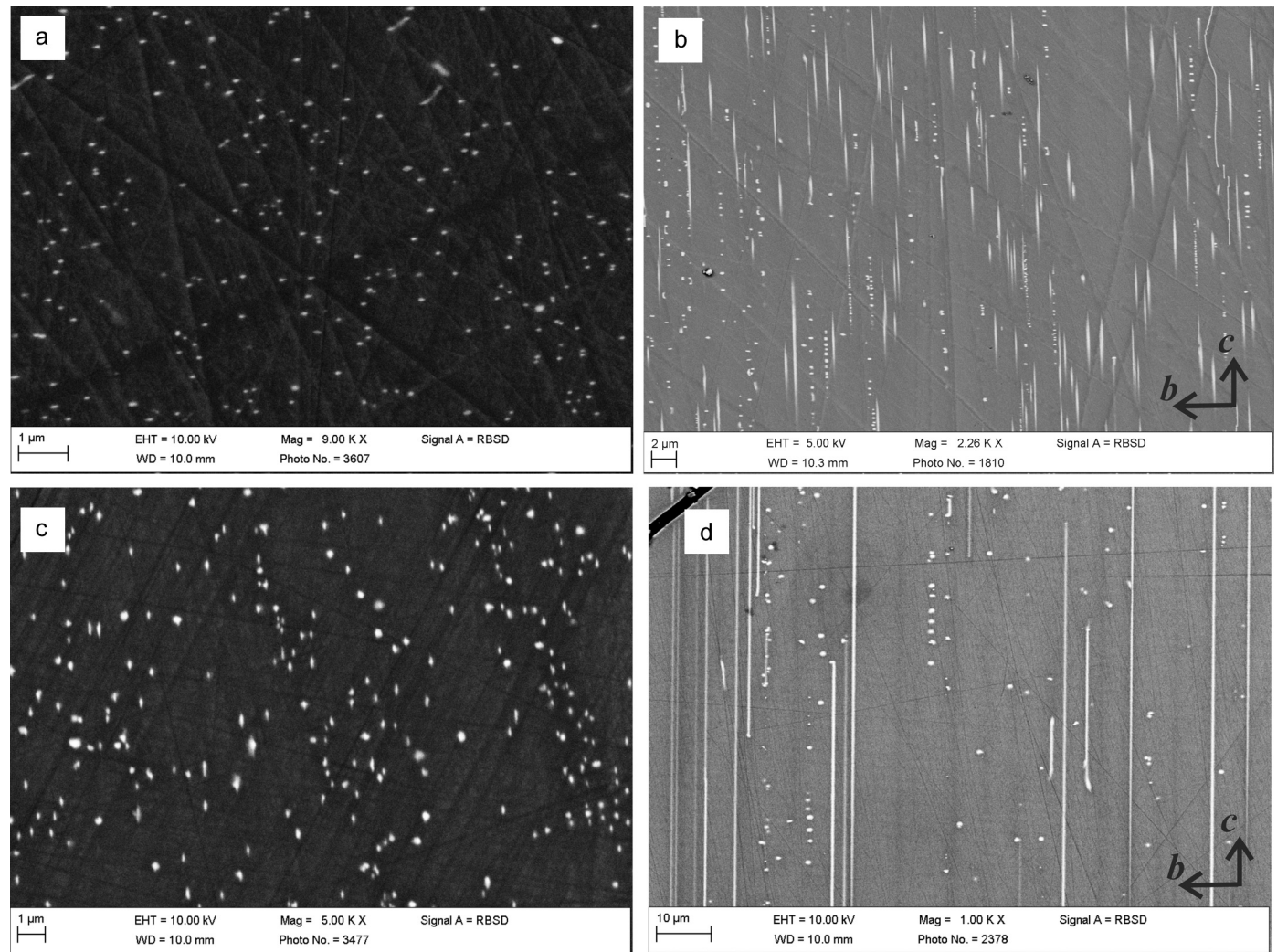


Fig. 3. BEIs showing the initial dislocation structures. The crystallographic axes are shown by arrows in b) and d). a) α -deformed sample on the (001) plane. b) α -deformed sample on the (100) plane. c) ϵ -deformed sample on the (001) plane. d) ϵ -deformed sample on the (100) plane.

after deformation and before annealing. These images show that dislocations appear mainly as dots on the (001) plane and mainly as lines on the (100) plane in both slip directions. That is, the dis-

location lines are elongated in the [001] direction in both slip systems. For this reason, the dislocation densities are counted using the images on the (001) plane in both kinds of samples. Because

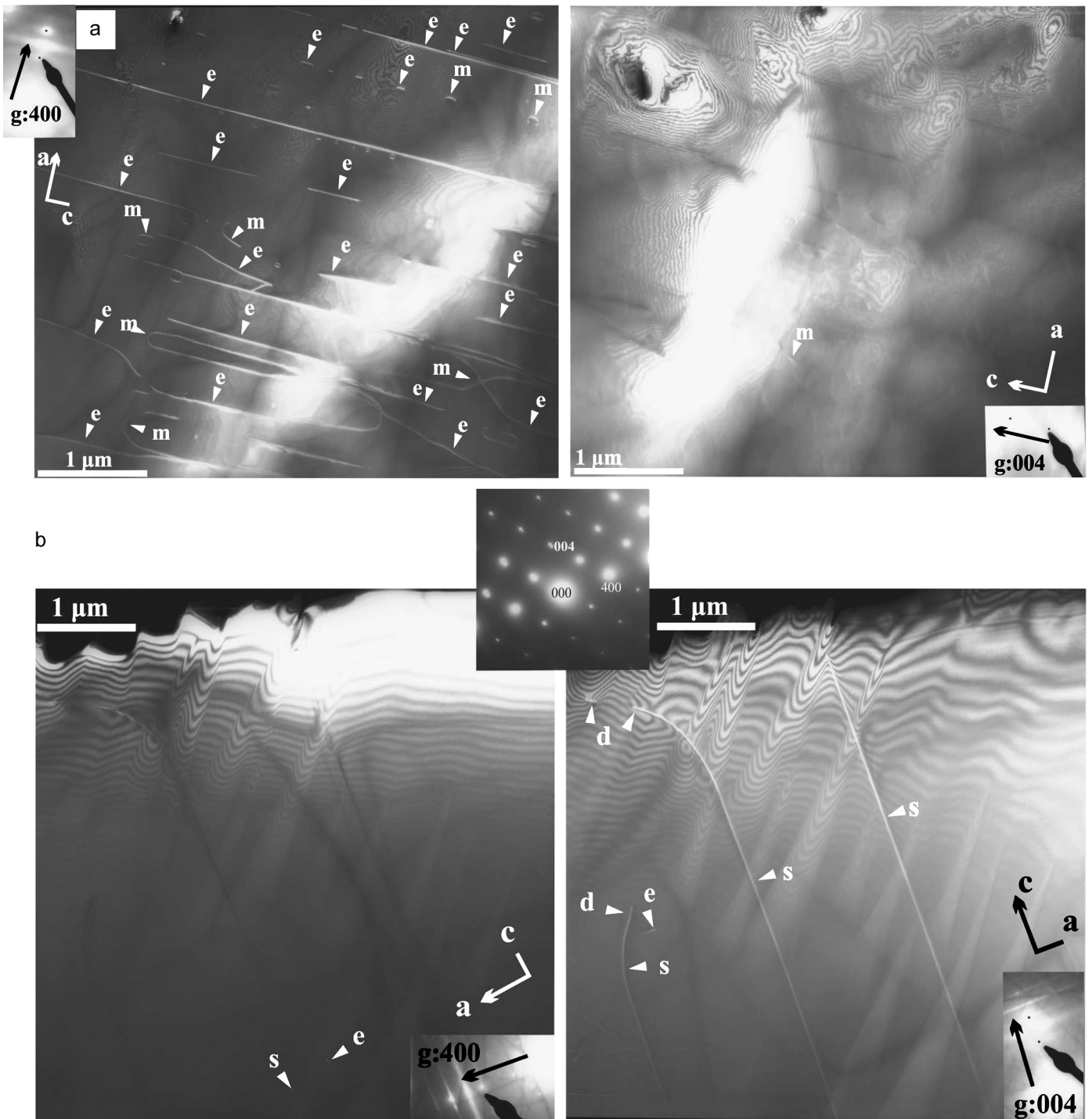


Fig. 4. TEM images showing the initial dislocation structures. a) WBDF images with $g = 400$ (left) and $g = 004$ (right) showing microstructures of **a**-slip sample (Z1054). Insets are SAED patterns showing the diffraction condition and the main axes (top left and bottom right) in the WBDF conditions. b) WBDF image with $g = 400$ (left) and $g = 004$ (right) showing microstructures of **c**-slip sample (Z1031). Insets are SAED patterns showing the nearest zone axis (on top) and the diffraction conditions with the principal crystal axes (bottom right) in each WBDF image.

the slip directions are $[100]$ and $[001]$ in the **a**- and **c**-slips, respectively, the dislocations produced by these slip systems should be $[100]$ edge and $[001]$ screw dislocations, respectively. Hereafter, the dislocations produced by the **a**- and **c**-slips are called **a**- and **c**-dislocations, respectively.

TEM observations confirmed the presence of mainly **a**- or **c**-dislocations in the crystals deformed in the $[100]$ or $[001]$ shear directions, respectively (Fig. 4). We measured the length of edge and screw dislocations and assuming the thickness of the TEM

foil as 100 nm to calculate the dislocation density. We also use Ham's (1961) method to measure the density of edge and screw dislocation. For the **a**-slip sample (Z1054), 93% of the dislocations were found to have Burgers vector in the $[100]$ direction, 74% of which were edge dislocations (Fig. 4a) with the dislocation density as $1.4 \mu\text{m}^{-2}$ (using total length of the edge dislocation divided by volume) and $1.6 \mu\text{m}^{-2}$ (using Ham, 1961 method). For the **c**-slip sample (Z1031), 94% of the dislocations were found to have Burgers vector of $[001]$, 57% of which were screw dislocations (Fig. 4b),

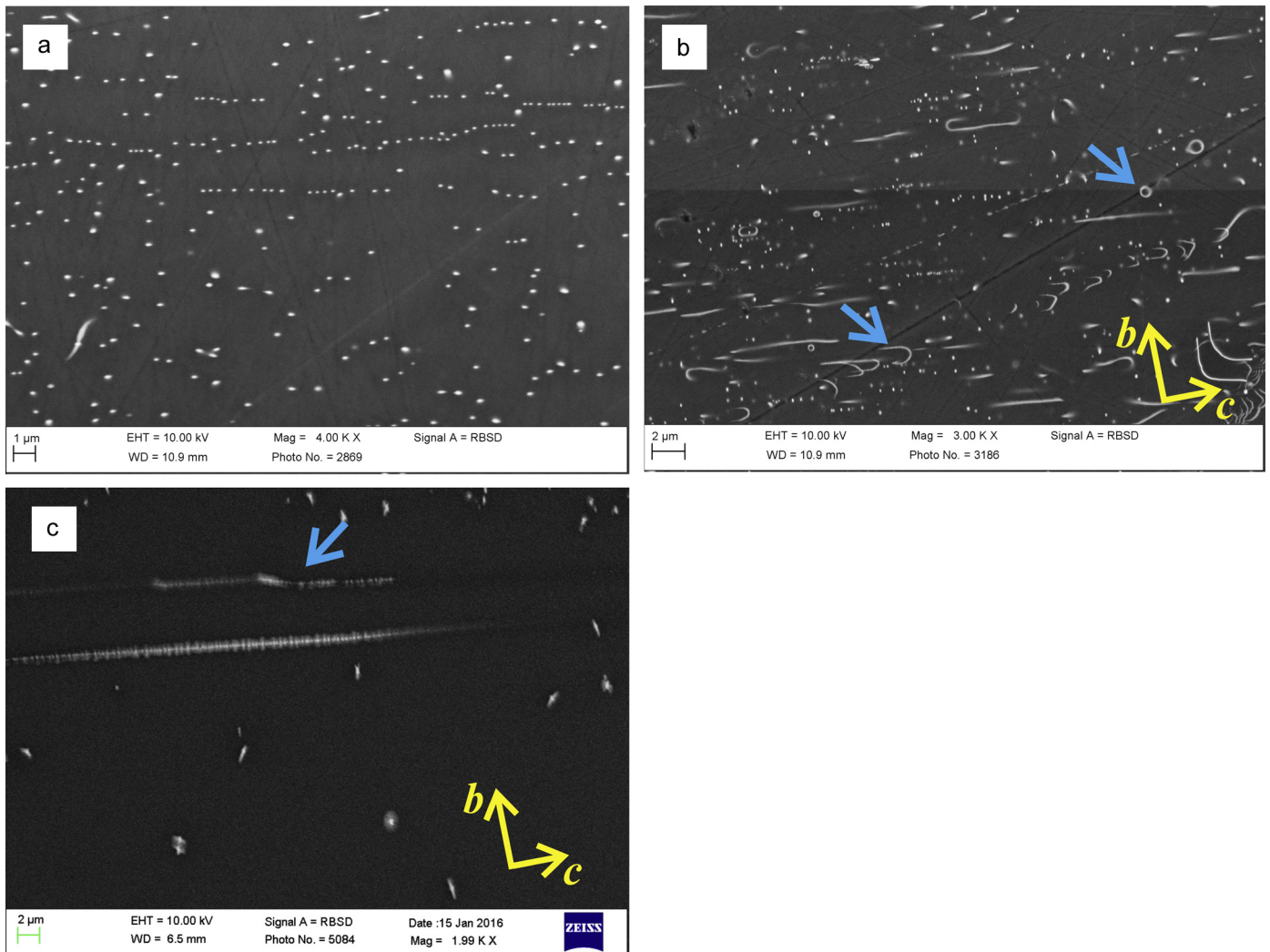


Fig. 5. BEIs showing the dislocation structures after annealing. a) α -deformed sample annealed at 1748 K for 20 min on the (001) plane. Alignment of edge dislocations occurred. b) α -deformed sample annealed at 1400 °C for 20 min observed on the (100) plane. Larger arrows indicate curved dislocation and dislocation loop. The crystallographic axes are shown by smaller arrows in b). c) c -deformed sample annealed at 1490 °C for 25 min observed on the (100) plane. The arrow points to a bent dislocation line indicating cross slip occurred during annealing. The crystallographic axes are shown.

with the dislocation density as $0.12 \mu\text{m}^{-2}$ (using total length of the screw dislocation divided by volume) and $0.26 \mu\text{m}^{-2}$ (using Ham, 1961 method).

The water content of olivine after deformation is below the detection limit by infrared spectroscopy. We didn't determine the water content after annealing, expecting it is nearly zeros since the annealing was held at room pressure and high temperature.

Fig. 5 shows the decorated dislocations after annealing. The decrease in dislocation density and formation of dislocation arrays were observed after annealing (Fig. 5a). Changes in dislocation density in areas away from the dislocation arrays were measured to prevent the formation of the dislocation arrays from influencing the dislocation annihilation. The curved dislocation structures after annealing suggest that dislocation climb occurred during recovery for edge dislocations (Fig. 5b). The bent dislocation lines (Fig. 5c) indicate that cross slip occurred during recovery of screw dislocations.

Fig. 6 plots the logarithmic of rate constant of dislocation annihilation against the reciprocal temperature. The results from the previous dislocation recovery experiments on olivine single crystal are also plotted in this figure. The dislocation annihilation rate constant of a -dislocations and c -dislocations are comparable, but those for the c -dislocations are half an order of magnitude

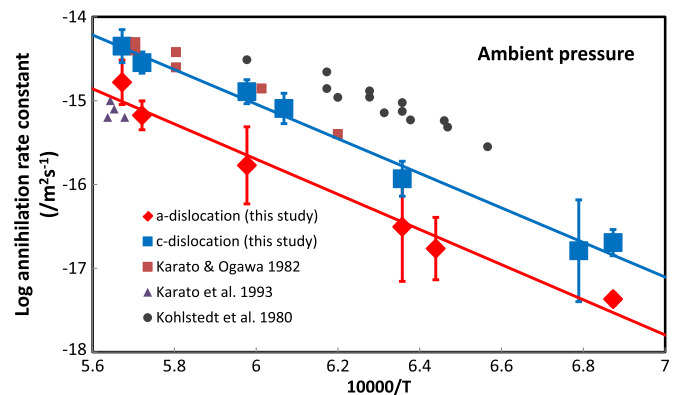


Fig. 6. Logarithmic dislocation annihilation rate constant of a - and c -dislocations (red diamonds and blue squares, respectively) versus the reciprocal temperature. No transition between a - and c -slip dislocation mobility occurs. Black circles: Kohlstedt et al. (1980); brown squares: Karato and Ogawa (1982); violet triangles: Karato et al. (1993). (For interpretation of the references to color in this figure legend, the reader is referred to the web version of this article.)

higher than those for the a -dislocations. The temperature dependences of the dislocation annihilation rate constants for the a - and c -dislocations are identical. The activation energies calculated

for the dislocation annihilation rate constant, which in this study are considered identical to those of the dislocation mobility, are $E_a = 400 \pm 20$ and $E_c = 400 \pm 30$ kJ/mol for **a**- and **c**-dislocations, respectively.

4. Discussion

4.1. Comparison with previous studies

Karato and Ogawa (1982) obtained an activation energy of 400 ± 60 kJ/mol for the dislocation annihilation rate constant. This value is reproduced in this study. The experiment by Kohlstedt et al. (1980) gave an activation energy of 300 ± 15 kJ/mol for the annihilation rate constant of natural and deformed olivine single crystal. However, we notice that the temperature range in Kohlstedt et al. (1980) was only 150 K. Karato et al. (1993) studied the pressure dependence of dislocation mobility, in which they adopted a similar activation energy (290 kJ/mol) to correct the difference in temperature conditions for their data points. Farla et al. (2011) gave an activation energy of 355 ± 81 kJ/mol for annihilation rate constant on San Carlos olivine polycrystals, which also agree to the present results within the margin of error.

The rate constants of **a**-dislocations from this study are comparable with those from Karato et al. (1993), which used the same technique to study the recovery of **a**-dislocations. The results from Kohlstedt et al. (1980) and Karato and Ogawa (1982) are similar to or slightly higher than the rate constants of **c**-dislocations in this study. Although the dislocation characters were not characterized in these studies, both **a**- and **c**-dislocations should be present because their samples were deformed in the $[101]_c$ direction. Therefore, the values of previous single crystal work should reflect the average rate constant for both slip systems. The somewhat larger rate constants may be due to the different techniques employed to observe dislocations in their studies (TEM by Kohlstedt et al., 1980, optical microscopy by Karato and Ogawa, 1982). The TEM method is restricted by the limited sampling area, which cannot give a statistical average when calculating dislocation density. Optical microscopy potentially underestimates dislocation density when it is high, which applies equally to the initial and annealed dislocation densities, resulting in a lower annihilation rate constant through Eq. (2) (Farla et al., 2011). The rate constants obtained from polycrystalline olivine by Farla et al. (2011) are two orders of magnitude lower than those in this study. This might be due to pinning the dislocation on grain boundaries and tangling dislocations of different types in their experiments.

The olivine single crystal starting material used in this study is not mantle origin and the trace element abundance is somewhat different from mantle derived olivine (Gose et al., 2010). However, the similar annihilation rate constant of our study and Karato et al., 1993 (see our Fig. 6) indicate dislocation interactions and annihilation, which is defect assisted, does not change significantly between Pakistan olivine and San Carlos olivine. In addition, the water content after deformation is below the detect limit of infrared spectrometry. Therefore, we do not think the composition difference between the olivine we used and mantle derived olivine alter the results.

4.2. Comparison of results with other techniques

The microstructures of dislocation after annealing indicate climb occurred for edge dislocation and cross slip occurred for screw dislocation. In addition, since they are the slower process compared to dislocation glide, we think the activation energy we obtain for annihilation represent that of dislocation climb for **a**-dislocation and cross slip for **c**-dislocation. The activation energies obtained in this study are identical to that for the Si

self-diffusion given by Fei et al. (2012) (410 ± 30 kJ/mol), within the margin of error. The identical activation energies for dislocation mobility and Si diffusion suggest that the dislocation climb in edge dislocation and cross slip in screw dislocation in dislocation recovery are controlled by Si self-diffusion. The identical activation energies for both **a**- and **c**-dislocations also support this idea.

In contrast, deformation experiments on dry polycrystalline olivine typically yield higher activation energies, namely about 500 kJ/mol (Goetze, 1978; Karato and Jung, 2003; Hirth and Kohlstedt, 2003), than those of dislocation mobility (this study; Kohlstedt et al., 1980; Karato and Ogawa, 1982; Karato et al., 1993; Farla et al., 2011). This discrepancy suggests that dislocation creep in the deformation experiments is likely driven by a combination of mechanisms. The stress levels in the deformation experiment are generally higher, in the order of 100 MPa to 1 GPa, and the deformation mechanism in such experiments is at the boundary of Peierls mechanism and the dislocation power law creep (e.g., Jung and Karato, 2001; Karato and Jung, 2003). Therefore, dislocation glide should be a significant component in the deformation experiments, but not in the dislocation recovery experiments.

4.3. Geophysics application

Whether temperature can cause the fabric transition between A- and B-type is determined by the activation energy of creep caused by **a**-dislocation and **c**-dislocation, which are constrained by the rate limiting process of **a**- and **c**-dislocations movement, i.e. climb or cross-slip. We found the same activation energy for the annihilation rate of **a**- and **c**-dislocations and think they represent the activation energy of dislocation climb and cross slip for **a**- and **c**-dislocations. Therefore, the fabric transition between A- and B-type cannot be caused by temperature.

In order to investigate the strain rate caused by **a**- and **c**-dislocations, we need to know the relationship between the dislocation climb (cross slip) velocity and the average dislocation velocity. The function of force ($f(\text{force})$) which acting on the dislocation per unit length is also need to link the dislocation climb (cross slip) mobility (k), which is investigated in this study, and climb (cross slip) velocity (v), since

$$v = k \cdot f(\text{force}) \quad (4)$$

Recent work on simulation of dislocation movement in olivine (Boioli et al., 2015) suggested a constant ratio between dislocation glide velocity and average mobile dislocation velocity. However, we noticed that at low stress condition (less than 5 MPa in their Fig. 9), their average mobile dislocation velocity is nearly the same as climb velocity. Therefore, we can use dislocation climb velocity to represent average mobile dislocation velocity at low stress conditions when climb is the rate limiting process for creep. If we assume that dislocation cross slip velocity is also similar to the average mobile dislocation velocity at low stress conditions when cross slip is the rate limiting process for creep, and the force function is the same for climb and cross slip process, the strain rate produced by **a**- and **c**-dislocation would be same. Therefore, at such conditions, we can use our result to infer the creep caused by **a**- and **c**-dislocations at low stress conditions. Here, we emphasize that only when the two assumptions are met, 1) dislocation cross slip velocity is similar to the average mobile dislocation velocity at low stress conditions when cross slip is the rate limiting process for creep. 2) The force functions are the same for climb and cross slip are the same, can we use our result to infer the strain rate caused by these two slip systems.

In low-stress regions, such as oceanic mantle (0.1 to 1 MPa, Hirth and Kohlstedt, 2003), we assume that the two assumptions mentioned above are met and then the strain rate caused by **a**- and **c**-slips should be comparable mobile in the deformation

of olivine in oceanic mantle and, accordingly, the AG-type fabric could dominate. Indeed, some natural mantle rocks, such as olivine from the Hilti mantle section (Michibayashi and Mainprice, 2004) and olivine from the Pannonian Basin (Hidas et al., 2007), show AG-fabric. Recently, Tommasi and Vauchez compiled the LPOs of natural olivine and showed a considerable amount of AG-fabric (Tommasi and Vauchez, 2015). This further confirms the existence of the AG-type fabric. Such fabric could be formed by the non-coaxial flow in the lithospheric mantle, close to Moho (Hilti mantle section after Michibayashi and Mainprice, 2004) or at the fossil lithospheric–asthenospheric boundary (Pannonian Basin, Hidas et al., 2007) or related to the type of strain (Higgins and Tommasi, 2012). The present results, however, provide a new insight to the formation of AG-type, i.e. it is due to the comparable dislocation mobility in the *a*- and *c*-slips at low stresses.

The dominance of AG-type fabric in the oceanic asthenosphere is also suggested by the seismic studies. The oceanic asthenosphere is not only characterized by azimuthal S wave anisotropy but also by stronger P wave and S wave radial anisotropy (e.g. Gung et al., 2003; Nettles and Dziewoński, 2008). However, none of the fabric shown in deformation experiment reproduces the comparably stronger radial anisotropy than azimuthal anisotropy (Song and Kawakatsu, 2012). Instead, the AG type olivine fabric can produce such character since the strong alignment of [010] axis and the diffusive distribution of [100] and [001] axis in the (010) plane. Assuming the elastic tensor of orthorhombic symmetry in the subducting oceanic asthenosphere, which can be produced by AG-type olivine fabric, the SKS splitting patterns across the fore-arc in central Alaska are well explained (Song and Kawakatsu, 2013). Although existing of horizontal melt layer in asthenosphere could enhance the radial anisotropy (e.g. Kawakatsu et al., 2009), these layer might solidify during subduction. Therefore, AG-type olivine fabric might be a potential candidate to explain the seismic anisotropy in the oceanic asthenosphere.

In high stress region, such as lithosphere and convergent boundaries, the average mobile dislocation velocity deviates a lot from dislocation climb velocity (Boioli et al., 2015) and we cannot use dislocation climb (cross-slip) velocity to represent average mobile dislocation velocity dislocation. Since glide contributes considerably to deformation, as in the deformation experiments, A- and B-type fabrics form.

The change from A- or B-type fabric to AG-type fabric with decreasing stress may provide a new explanation for the decrease in seismic anisotropy with depth. AG-type fabric produces weaker seismic anisotropy than A- or B-types fabric. Olivine has the highest P-wave velocity in the *a*-direction. For S waves, the highest velocity occurs when oscillation is in the *a*-direction. Therefore, A- or B-type fabric should produce strong P-wave azimuthal anisotropy. On the other hand, the AG-type fabric produces no or weak P-wave azimuthal anisotropy, because the direction of the *a*-axis is not concentrated, but distributed on the flow plane. A similar situation exists for S-wave anisotropy. Therefore, the decrease in seismic anisotropy with depth in the upper mantle down to 300 km depth might be caused by transition of olivine from A- or B-type to AG-type, due to decrease in stress with depth.

Finally, we must emphasize that our explanation about the origin of AG-type fabric is based on the two assumptions mentioned above, which need to be tested in the future. In addition, our result is based on the experiments conducted on the single crystal. The results might change in the case of polycrystalline material, which dislocation mobility might be influenced by grain boundary.

5. Conclusion

The present study shows that the dislocation annihilation rates for the [100](010) edge dislocation are slightly smaller than those

for the [001](010) screw dislocation. The temperature dependences of climb in [100] edge dislocation and cross slip in [001] screw dislocations are identical: their activation energies are both 400 kJ/mol. Therefore, fabric transition due to temperature is unlikely. The identical activation energies of dislocation movement and Si self-diffusion suggest that the dislocation climb/cross slip is controlled by Si diffusion. The discrepancy between the activation energies for the deformation experiment and recovery experiment may be due to high stresses in deformation experiments. Under certain assumptions, we can use our result to infer the creep caused by *a*- and *c*-dislocations at low stress conditions. If so, under low-stress conditions, like the oceanic mantle, the AG-type fabric may dominate, while A- or B-type fabric forms under high-stress conditions, like the lithosphere and convergent boundaries. The transition from A- or B-type fabric to AG-type fabric with decreasing stress may be the reason for the decrease in seismic anisotropy with depth.

Acknowledgements

We acknowledge F. Heidelbach and P. O'Brien for providing the olivine single crystals and T. Boffa-Ballaran for instructing the single crystal X-ray diffractometry. We thank technicians in BGI for the sample and assembly preparation. This research was supported by DFG grants to TK (KA3434/3-1, KA3434/7-1, KA3434/8-1 and KA3434/9-1) and by the annual budget of Bayerisches Geoinstitut.

References

- Angel, R.J., Finger, L.W., 2011. SINGLE: a program to control single-crystal diffractometers. *J. Appl. Crystallogr.* 44, 247–251.
- Ben Ismail, W., Mainprice, D., 1998. An overview of upper mantle fabrics and seismic anisotropy. *Tectonophysics* 296, 145–157.
- Boioli, F., Carrez, P., Cordier, P., Devincere, B., Marquille, M., 2015. Modeling the creep properties of olivine by 2.5-dimensional dislocation dynamics simulations. *Phys. Rev. B* 92, 014115.
- Dobrzynetskaia, L., Green II, H.W., Wang, S., 1996. Alpe Arami: a peridotite massif from depths of more than 300 kilometers. *Science* 271, 1841–1845.
- Dziewoński, A.M., Anderson, D.L., 1981. Preliminary reference Earth model. *Phys. Earth Planet. Inter.* 25, 297–356.
- Farla, R.J.M., Kokkonen, H.K., Fitz Gerald, J.D., Barnhoorn, A., Faul, U.H., Jackson, J., 2011. Dislocation recovery in fine-grained polycrystalline olivine. *Phys. Chem. Miner.* 38, 363–377.
- Fei, H., Hegoda, C., Yamazaki, D., Wiedenbeck, M., Yurimoto, H., Shcheka, S., Katsura, T., 2012. High silicon self-diffusion coefficient in dry forsterite. *Earth Planet. Sci. Lett.* 345, 95–103.
- Goetze, C., 1978. Mechanisms of creep in olivine. *Philos. Trans. R. Soc. Lond.* 288, 99–119.
- Goetze, G., Kohlstedt, D.L., 1973. Laboratory study of dislocation climb and diffusion in olivine. *J. Geophys. Res.* 78, 5962–5970.
- Gose, J., Schmädicke, E., Markowitz, M., Beran, A., 2010. OH point defects in olivine from Pakistan. *Mineral. Petrol.* 99, 105–111.
- Gung, Y., Panning, M., Romanowicz, B., 2003. Global anisotropy and the thickness of continents. *Nature* 422, 707–711.
- Ham, R.K., 1961. The determination of dislocation densities in thin films. *Philos. Mag.* 6, 1183–1184.
- Hidas, K., Falus, Gy., Szabó, Cs., Szabó, P.J., Kovács, I., Földes, T., 2007. Geodynamic implications of flattened tabular equigranular textured peridotites from the Bakony–Balaton Highland Volcanic Field (Western Hungary). *J. Geodyn.* 43, 484–503.
- Higgie, K., Tommasi, A., 2012. Feedbacks between deformation and melt distribution in the crust–mantle transition zone of the Oman ophiolite. *Earth Planet. Sci. Lett.* 359, 61–72.
- Hirth, G., Kohlstedt, D., 2003. Rheology of the upper mantle and the mantle wedge: a view from the experimentalists. In: *Inside the Subduction Factory*. *Geophys. Monogr.*, vol. 138, pp. 83–105.
- Holtzman, B.K., Kohlstedt, D.L., Zimmerman, M.E., Heidelbach, F., Hiraga, T., Hustoft, J., 2003. Melt segregation and strain partitioning: implications for seismic anisotropy and mantle flow. *Science* 301, 1227–1230.
- Hull, D., Bacon, D.J., 2011. *Introduction to Dislocations*. Elsevier, 257 pp.
- Jung, H., Karato, S.I., 2001. Water-induced fabric transitions in olivine. *Science* 293, 1460–1463.
- Jung, H., Katayama, I., Jiang, Z., Hiraga, T., Karato, S.I., 2006. Effect of water and stress on the lattice-preferred orientation of olivine. *Tectonophysics* 421, 1–22.

- Karato, S., 1987. Scanning electron microscope observation of dislocations in olivine. *Phys. Chem. Miner.* 14, 245–248.
- Karato, S., 1988. The role of recrystallization in the preferred orientation of olivine. *Phys. Earth Planet. Inter.* 51, 107–122.
- Karato, S., 2008. *Deformation of Earth Materials: Introduction to the Rheology of the Solid Earth*. Cambridge Univ. Press, Cambridge, UK. 462 pp.
- Karato, S., Jung, H., 2003. Effects of pressure on high-temperature dislocation creep in olivine. *Philos. Mag.* 83, 401–414.
- Karato, S., Ogawa, M., 1982. High-pressure recovery of olivine: implications for creep mechanisms and creep activation volume. *Phys. Earth Planet. Inter.* 28, 102–117.
- Karato, S., Rubie, D.C., Yan, H., 1993. Dislocation recovery in olivine under deep upper mantle conditions: implications for creep and diffusion. *J. Geophys. Res.* 98, 9761–9768.
- Katayama, I., Jung, H., Karato, S.I., 2004. New type of olivine fabric from deformation experiments at modest water content and low stress. *Geology* 32, 1045–1048.
- Katayama, I., Karato, S., 2006. Effect of temperature on the B- to C-type olivine fabric transition and implication for flow pattern in subduction zones. *Phys. Earth Planet. Inter.* 157, 33–45.
- Kawakatsu, H., Kumar, P., Takei, Y., Shinohara, M., Kanazawa, T., Araki, E., Suyehiro, K., 2009. Seismic evidence for sharp lithosphere–asthenosphere boundaries of oceanic plates. *Science* 324, 499–502.
- Kohlstedt, D.L., Goetze, C., Durham, W.B., Vandersande, J., 1976. New technique for decorating dislocations in olivine. *Science* 191, 1045–1046.
- Kohlstedt, D.L., Nichols, H.P.K., Hornack, P., 1980. The effect of pressure on the rate of dislocation recovery in olivine. *J. Geophys. Res.* 85, 3122–3130.
- Li, J.C.M., 1966. Recovery processes in metals. In: *Recrystallization, Grain Growth and Textures*. Am. Soc. Metals, pp. 45–63.
- Mainprice, D., 2007. Seismic anisotropy of the deep Earth from a mineral and rock physics perspective. In: Schubert, G. (Ed.), *Treatise on Geophysics*. Elsevier, Oxford, pp. 437–492.
- Michibayashi, K., Mainprice, D., 2004. The role of pre-existing mechanical anisotropy on shear zone development within oceanic mantle lithosphere: an example from the Oman ophiolite. *J. Petrol.* 45, 405–414.
- Mizukami, T., Wallis, S.R., Yamamoto, J., 2004. Natural examples of olivine lattice preferred orientation patterns with a flow-normal a-axis maximum. *Nature* 427, 432–436.
- Montagner, J.P., Kennett, B.L.N., 1996. How to reconcile body-wave and normal-mode reference Earth models. *Geophys. J. Int.* 125, 229–248.
- Nettles, M., Dziewoński, A.M., 2008. Radially anisotropic shear velocity structure of the upper mantle globally and beneath North America. *J. Geophys. Res.* 113, 1978–2012.
- Nicolas, A., Bouchez, J.L., Boudier, F., Mercier, J.-C.C., 1971. Textures, structures and fabrics due to solid state flow in some European lherzolites. *Tectonophysics* 12, 55–86.
- Ohuchi, T., Kawazoe, T., Nishihara, Y., Nishiyama, N., Irifune, T., 2011. High pressure and temperature fabric transitions in olivine and variations in upper mantle seismic anisotropy. *Earth Planet. Sci. Lett.* 304, 55–63.
- Poirier, J.P., Vergobbi, B., 1978. Splitting of dislocations in olivine, cross slip-controlled creep and mantle rheology. *Phys. Earth Planet. Inter.* 16, 370–378.
- Satsukawa, T., Michibayashi, K., Anthony, E.Y., Stern, R.J., Gao, S.S., Liu, K.H., 2011. Seismic anisotropy of the uppermost mantle beneath the Rio Grande rift: evidence from Kilbourne Hole peridotite xenoliths, New Mexico. *Earth Planet. Sci. Lett.* 311, 172–181.
- Skemer, P., Katayama, I., Karato, S.I., 2006. Deformation fabrics of the Cima di Gagnone peridotite massif, Central Alps, Switzerland: evidence of deformation at low temperatures in the presence of water. *Contrib. Mineral. Petrol.* 152, 43–51.
- Song, T.R.A., Kawakatsu, H., 2012. Subduction of oceanic asthenosphere: evidence from sub-slab seismic anisotropy. *Geophys. Res. Lett.* 39, L17301.
- Song, T.R.A., Kawakatsu, H., 2013. Subduction of oceanic asthenosphere: a critical appraisal in central Alaska. *Earth Planet. Sci. Lett.* 367, 82–94.
- Tommasi, A., Vauchez, A., 2015. Heterogeneity and anisotropy in the lithospheric mantle. *Tectonophysics* 661, 11–37.
- Toriumi, M., Karato, S.I., 1978. Experimental studies on the recovery process of deformed olivines and the mechanical state of the upper mantle. *Tectonophysics* 49, 79–95.
- Visser, K., Trampert, J., Lebedev, S., Kennett, B.L.N., 2008. Probability of radial anisotropy in the deep mantle. *Earth Planet. Sci. Lett.* 270, 241–250.